Article

Modelling Past Tsunamis in European Waters

Raúl Periáñez [1],*, José María Abril [1] and Carmen Cortés [2]

[1] Department of Applied Physics I, University of Seville, 41013 Seville, Spain

[2] Department of Applied Mathematics I, University of Seville, 41013 Seville, Spain

* Correspondence: rperianez@us.es

Abstract: A research model to simulate the propagation of tsunamis caused by different mechanisms was developed in this paper. These mechanisms are submarine earthquakes, landslides and collapse of volcano calderas. The model is based upon the non-linear shallow-water hydrodynamic equations with horizontal viscosity and friction with the seabed. It also includes a flooding/drying algorithm. This model was tested by applying it to several past tsunamis and comparisons of results with available data and/or other models. The objective of this paper is to present a summary on the application of the model to historical tsunamis occurred in European waters: Atlantic Ocean, Mediterranean Sea and Caspian Sea. Additionally, two application examples on how the research model can be used to confront different candidate tsunami sources and to discard scenarios of catastrophic floodings initially attributed to tsunamis presented: the Santorini tsunami sequence and the flooding of the Gulf of Tartessos in SW Spain.

Keywords: numerical mode; earthquake; landslide; volcano calder; tsunami; European seas

1. Introduction

The numerical simulation of tsunamis has attracted attention, specially after the large tsunamis in the Indian Ocean in 2004 and the east Japan tsunami in 2011, which in addition led to the accident in Fukushima Daiichi nuclear power plant.

Tsunamis may be generated by a number of mechanisms, like submarine and subaerial landslides, fall of asteroids into the sea, collapse of volcano calderas or submarine earthquakes. An overview on the dynamics of tsunami waves can be seen, for instance, in the paper [1]. The numerical modelling of tsunamis is a complex task involving several spatio-temporal scales, from the tsunami generation and propagation in the sea to interactions with the shoreline, subsequent flooding of the land where interactions with vegetation, buildings, etc., may occur.

A number of tsunami models are available (this can be seen for instance in the recent review by Marras and Mandli [2]). There are also other models not mentioned in this review, as for instance JAGURS and VOLNA models [3,4]. These models differ in their structure (from one-dimensional to fully three-dimensional models), equations, turbulence schemes (if considered), inclusion of wave breaking or not, and interactions with land structures. Most models do not have the capability of describing erosion and sediment transport, although some of them do [5].

Together with these operational models, many research models have been developed and applied by different institutions. These research models offer the flexibility to use alternative descriptions of processes and their results may be tested with observational data and/or results of other models taking the Lisbon tsunami in 1755, the 2004 Indian Ocean tsunami, and tsunami in the Pacific Ocean as examples [6–8].

A hydrodynamic model was fully developed by the University of Seville. It was applied to a number of problems such as tide propagation, density-driven circulation, sediment transport, pollutant transport, floodings and also tsunami propagation. Thus, it is a complete and flexible tool which can be adapted and customized to a large number of hydrodynamic problems and different marine environments. The purpose of this paper is to present a summary of the applications of such research model to historical tsunamis caused by submarine earthquakes, a landslide and a caldera collapse in European waters (Atlantic Ocean, Mediterranean Sea and Caspian Sea).

Although very sophisticated operational models exist [2], in some cases there is not enough information to implement them, just like in the case of historical tsunamis. Some practical applications of the present model approach are hard to handle with such operational models: (i) confrontation of several candidate sources (e.g. Lisbon tsunami, Santorini tsunami sequence including the origin of the thick megaturbidite in the Ionian Abyssal Plain-known as the Augias megaturbidite), (ii) the discard of some unlikely scenarios of catastrophic floods attributed to tsunamis, and (iii) preliminary risk assessment of potential tsunamigenic sources. In these cases a flexible research model presented in this paper may be of practical utility.

The model is described in Section 2. Examples of its application to some of the problems mentioned in the paragraph above are presented in Section 3.

2. Tsunami Modelling

The model is based on the 2D shallow-water equations. They describe the propagation of surface shallow-water gravity waves. This approximation implies that wave length is longer than water depth, which is generally the case in this kind of applications. The model includes non–linear terms, Coriolis term due to rotation of the Earth and dissipation due to horizontal viscosity and friction with the seabed. These equations (Equations (1)–(3)) are:

$$\frac{\partial \zeta}{\partial t} + \frac{\partial}{\partial x}(Hu) + \frac{\partial}{\partial y}(Hv) = 0 \tag{1}$$

$$\frac{\partial u}{\partial t} + u\frac{\partial u}{\partial x} + v\frac{\partial u}{\partial y} + g\frac{\partial \zeta}{\partial x} - \Omega v + \frac{\tau_u}{\rho H} = A\left(\frac{\partial^2 u}{\partial x^2} + \frac{\partial^2 u}{\partial y^2}\right) \tag{2}$$

$$\frac{\partial v}{\partial t} + u\frac{\partial v}{\partial x} + v\frac{\partial v}{\partial y} + g\frac{\partial \zeta}{\partial y} + \Omega u + \frac{\tau_v}{\rho H} = A\left(\frac{\partial^2 v}{\partial x^2} + \frac{\partial^2 v}{\partial y^2}\right) \tag{3}$$

where u and v are the depth averaged water velocities along the x and y axis (eastwards and northwards respectively), h is water depth below the mean sea level, ζ is the displacement of the water surface with respect to the mean sea level, which is measured upwards, and $H = h + \zeta$ is defined as the total water depth. The Coriolis parameter is Ω ($\Omega = 2\omega \sin \lambda$; here ω is the rotational angular velocity of the Earth and λ is latitude), g is gravity acceleration, ρ is the mean water density and A is the horizontal eddy viscosity coefficient. Finally, τ_u and τ_v are the seabed friction stresses. These have been written using a quadratic law (Equation (4)):

$$\tau_u = k\rho\rho\sqrt{u^2 + v^2}$$
$$\tau_v = k\rho\rho\sqrt{u^2 + v^2} \tag{4}$$

where k is a bed friction coefficient. These equations essentially express mass and momentum conservation.

All the equations are solved using second order accuracy explicit finite difference schemes [9]. The exception is bed friction, which is written in a semi-implicit scheme. The MSOU (Monotonic Second Order Upstream) scheme is applied to the advective non-linear terms appearing in the momentum equations. A detailed description of this method is available [10]. The hydrodynamic component of the tsunami model has been validated, as mentioned in the Introduction, through its application to other problems in tide propagation [11–15] and density-driven circulation [16,17]. Of course, baroclinic terms are added to the equations in the last case.

Appropriate boundary conditions are required in order to restrict water flow towards a land grid cell. A flood/dry algorithm is applied as new wet or dry grid cells can be generated when the tsunami reaches the shoreline. The numerical scheme was used due to its relative simplicity [10]. Wet grid cells are defined as those which have a total water depth H larger than a threshold value H_{min}. This value is set as a few centimeters (in our studies H_{min} = 0.10 m was used). On the other hand, dry cells are defined as those where $H \leq H_{min}$. Wetting and drying is implemented in the code through the calculation of the water velocity component which is normal to the interface between wet and land cells. The calculation is carried out when the pressure gradient force (terms $g\frac{\partial \zeta}{\partial x}$ and $g\frac{\partial \zeta}{\partial y}$, Equations (2) and (3) respectively) is directed towards the land cell. Otherwise the velocity will be set to zero. If the velocity is non–zero, water level in the land cell increases. This methodology can be used to estimate the areas where flooding might occur, but cannot be interpreted as a detailed runup calculation since the grid resolutions are not fine enough for such purpose.

Open boundary conditions are also required. A gravity wave radiation condition (Equations (5) and (6)) is adopted for the sea elevation along such boundaries [18]. It is assumed that processes near the open boundaries are governed by outgoing waves. This is a valid approach since the tsunami propagates outside from inside the model domain. This boundary condition is used in an implicit form, thus:

$$\zeta(x_b, t+1) = \frac{\zeta(x_b, t) + \mu\zeta(x_{b-1}, t+1)}{1+\mu} \tag{5}$$

where $t + 1$ is the future time step, x_b gives the boundary location and x_{b-1} designs the location of the interior point which is the nearest to the open boundary. Finally,

$$\mu = c\frac{\Delta t}{\Delta x} \tag{6}$$

with $c = \sqrt{gH}$ which is the shallow-water barotropic phase speed, Δx is model spatial resolution and Δt is the time step used to integrate the equations. Information transit across the open boundary without artificial reflection and/or amplification is allowed with this boundary condition. Actually, tsunamis may be considered as shallow–water waves since wavelength is larger than water depth.

For earthquake tsunamis, initial conditions in all the domain (except over the area affected by the deformation in the free water surface induced by the earthquake) consist of zero water elevations and velocities (so–called still water conditions). The floor deformation caused by the earthquake is calculated by using the Okada classical formulae [19] through a MATLAB script which can be download from the web (available online: https://es.mathworks.com/matlabcentral). Input required for this script is the following: fault plane strike, rake, dip, slip, epicenter location, fault length and width (a rectangular one is assumed), as well as fault centroid depth and magnitude of the earthquake.

Topography over the model domain is corrected due to subsidence or uplift because of the fault. This is done by adding the Okada deformation to the original topography. Then, in water cells, it is assumed that such deformation is transferred instantaneously to the free water surface. This is then imposed as the initial condition for the numerical simulation.

Sometimes the earthquake parameters required to calculate the Okada deformation are not available. In this case, some standard empirical scaling equations may be used to estimate lacking data. In particular, the scaling laws published by Wells and Coppersmith [20], between the fault size and slip with the earthquake magnitude, were used. These laws (Equations (7)–(9)) are:

$$\log L = 0.59 M_W - 2.44 \tag{7}$$

$$\log W = 0.32 M_W - 1.01 \tag{8}$$

$$\log S = 0.69 M_W - 4.80 \tag{9}$$

where L and W are the fault length and width (both in km). M_w is the earthquake magnitude and S is the average slip (in m) along the fault.

Scaling laws, which are specific for the different tectonic regimes of the considered earthquake, were recently proposed in the paper by Stirling et al. [21]. However, some of the required parameters are not provided by these specific laws. Thus, the general laws (which do not differentiate between tectonic regimes) given above [20] were used since they provide all the required parameters (fault length, width and slip) and, in addition, correlations between observed parameters and predictions are better than those obtained with scaling laws

which are specific for given tectonics. Nevertheless, it should be clearly noted that these empirical laws provide only approximations to the real fault characteristics.

In the case of a caldera collapse, waters are used as initial conditions again. In the area affected by the collapse the initial water level corresponds to the depth of the formed caldera. The initial water displacement is downwards (i.e., negative). This procedure has been successfully used in previous studies [22,23].

The method described by Tinti, Cecioni and Bellotti was used to simulate a submarine landslide [24,25]: the motion of the sea bottom is provided as input to the hydrodynamic equations. For that purpose, a term is added to the right side of the continuity equation (Equation (1)), which is given by Equation (10):

$$\frac{\partial h_s}{\partial t} \qquad (10)$$

where h_s designs the sea surface elevation due to the transit of the submarine landslide at a given point. This term constitutes the link between the landslide and the tsunami propagation model. The relation between h_s and the thickness of the slide H_s at the sea bottom is calculated through the use of a transfer function (Equations (11) and (12)):

$$\frac{\partial h_s}{\partial t} = \frac{\partial H_s}{\partial t} \frac{1}{\cosh(\alpha)} \qquad (11)$$

with

$$\alpha = \frac{2\pi H}{L_s} \qquad (12)$$

where H is water depth and L_s is the slide length. If the transfer function is not used, then we will obtain that $\partial h_s/\partial t = \partial H_s/\partial t$. This is a good approximation if the slide length is much larger than water depth. Through the use of the transfer function $1/\cosh \alpha$ we can attribute different potential to landslides of different L_s moving at different sea depths. Consequently, a shallow water slide has a higher capacity of generating waves ($\alpha \to 0$ and thus $\partial h_s/\partial t \approx \partial H_s/\partial t$) than if it moves in the deep ocean ($\alpha \gg 0$ and thus $\partial h_s/\partial t \ll \partial H_s/\partial t$).

The shape of the slide is represented by a box form of length L_s, width B and maximum thickness Δz. The edges of the box form are smoothed along both sides over a distance B from the central line, and in the front and rear end over a smoothing distance S by an exponential function with the purpose of avoiding sharp gradients in Δz. Full details can be found in the paper [26]. The slide volume is given by Equation (13) [26]:

$$V = 0.9B\Delta z(L_s + 0.9S) \qquad (13)$$

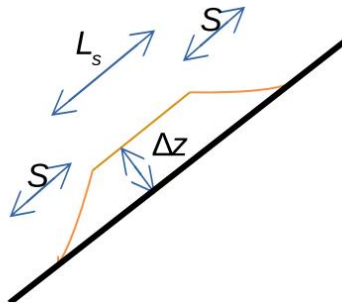where the number 0.9 is due to the smoothing. A side view of the slide is presented in Figure 1.

Figure 1. Schematic view of a submarine slide. L_s is the length, S is the smoothing distance in the front and rear and Δz the maximum slide thickness.

The model provides maps of wave amplitudes, maps of arrival times of the tsunami (defined as the arrival time of a 2 cm amplitude signal), time series of water elevation at desired locations and maps of maximum water current amplitudes induced by the tsunami.

Four model domains were used in this study: respectively for the Caspian Sea (CASP), the east Atlantic and western Mediterranean (coupled through the Strait of Gibraltar) (ATWMED), the central Mediterranean

(CEMED), and the eastern Mediterranean Sea (EASTMED). In all cases, topography was obtained from GEBCO08 digital atlas with a resolution of 30 s of arc in both longitude and latitude. Main characteristics of the domains and model parameters are given in Table 1. The time step, Δt, was selected to satisfy the CFL stability condition, given by Equation (14) [9]:

$$\Delta t < \frac{\Delta x}{\sqrt{gH_{max}}} \tag{14}$$

where H_{max} is the maximum water depth in each domain.

Table 1. Properties of the models (extension of the domains and time steps) used in the studies and values for eddy viscosity and bed friction coefficient.

	CASP	ATWMED	EASTMED	CEMED
Latitude	46.0° E–56.0° E	33.0° N–41.0° N	29.25° N–46.0° N	29.0° N–46.0° N
Longitude	36.0° N–47.5° N	13.0° W–6.0° E	22.0° E–36.25° E	9.33° E–22.0° E
Δt (s)	5	1	1	1
A (m^2/s)	10	10	10	10
k	0.0015	0.0025	0.0025	0.0025

The described hydrodynamic model has been applied to different problems mentioned above: tide propagation in a number of marine areas from local [11–13] to basin [14,15] and density-driven circulation calculations [16,17]; and also to other aspects of marine science such as sediment transport [16,27], pollutant transport [11–15] and floodings [28,29]. Thus, the hydrodynamic model is a complete and flexible tool which can be adapted and customized to a large number of hydrodynamic problems and different marine environments. This hydrodynamic model has been widely tested and validated by using field data (such as tidal elevations, phases, currents, pollutant concentrations, etc.), as shown in the references cited above.

3. Results

Some results obtained through the application of the model in this paper to several historical tsunamis are presented in this section. The model application to such tsunamis is useful to test if the model implementation to each domain is adequate. Essentially, it should be considered that there is not any field data to be used for comparison of model results, since the tsunamis are historical. Some historical notes could be found in some cases. Thus, we could only check whether model results were in qualitative agreement with such notes (if available) or with previous simulations made by other authors if such tsunami was previously studied. Full details are given in the references mentioned in each studied case. The geological characteristics of the areas under studies can be seen in specific papers and are not repeated here [30–33].

The focal mechanisms of the considered historical tsunamis are presented in Table 2. These parameters are used to calculate the initial Okada deformation, as explained before. Then the simulation of the tsunami propagation proceeds. In the cases of the landslide scenario and the volcano caldera collapse, the initial conditions are explained in each specific subsection (Sections 3.9 and 3.10 respectively).

Table 2. Focal mechanisms of the tsunamis simulated in this study. Appropriate references about these values are given along the text. D is the focal depth in km, longitude and latitude of the epicenter are given in degrees, L and W in km, the slip in m; and strike, dip and rake in degrees.

	M_w	D	Lon	Lat	L	W	Slip	Strike	Dip	Rake
1990	7.4	15	49.33	33.96	65	32	1.9	300	73	32
1895	7.8	20	53.7	39.5	110	40	3.8	292	80	−90
1755	8.5–9	5	−10.75	36.04	200	80	19	345	40	90
2003	6.9	6	3.64	36.89	60	24	0.71	70	45	90
1856	∼7	10	5.74	37.08	110	20	1.5	60	40	90
365AD	∼8.5	70	23.45	35.25	105	100	16	293	40	90
1222	7–7.5	15	32.50	34.50	50	25	3	305	35	110
1303	∼8	20	25.94	34.85	100	30	8	115	45	110

3.1. The 1755 Lisbon Tsunami

This tsunami was studied with the ATWMED model domain. In spite of the extensive work which has been carried out in the past by many researchers, [6,34,35] among others, the exact characteristics of its source are unknown. Several model runs were carried out and results in best agreement with the observational data from the date (some estimations of wave heights along the coast), the so-called source number 5 in Barkan et al. [35] (1755 tsunami in Table 2).

A map of the calculated wave amplitudes is presented in Figure 2. Most of the energy of the tsunami is directed towards the open Atlantic Ocean, although significant waves above 8 m reach the southwest coasts of Spain and Portugal. In particular, the highest waves arrive in the area of Cape San Vicente, where waves are concentrated due to bathymetry. It is interesting to note that the tsunami does not seem to enter the Mediterranean Sea, which is due to the dispersive effects in the narrow Strait of Gibraltar. This map is similar to that of the previous paper [35] (Figure 14 in reference [35]).
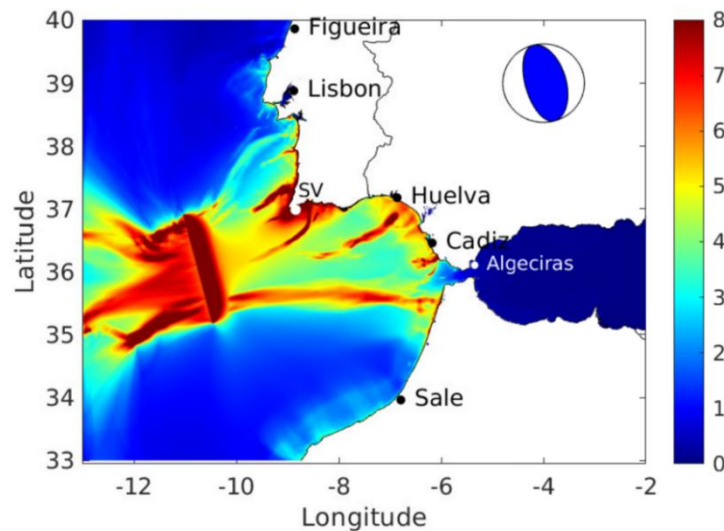

Figure 2. Computed wave amplitude (m) for the 1755 Lisbon tsunami. The beachball corresponding to the source is drawn. Locations where time series of elevations were obtained are indicated (SV means San Vicente Cape).

Time series of calculated water elevations at several locations in the domain are presented in Figure 3. Results are extracted from the model in the grid cell where each particular location is included. The mean water depth of such a grid cell is indicated in Figure 3 as well. It can be seen that several waves, about 4 m high, reached Lisbon. In contrast, a single wave followed by smaller sea level oscillations was apparent in places like San Vicente, Huelva, Sale and Cadiz. Such wave reached nearly 10 m in San Vicente and Cadiz, as well as a significant height, above 4 m, in Huelva and Sale. These results are in agreement with previous studies [6,35].
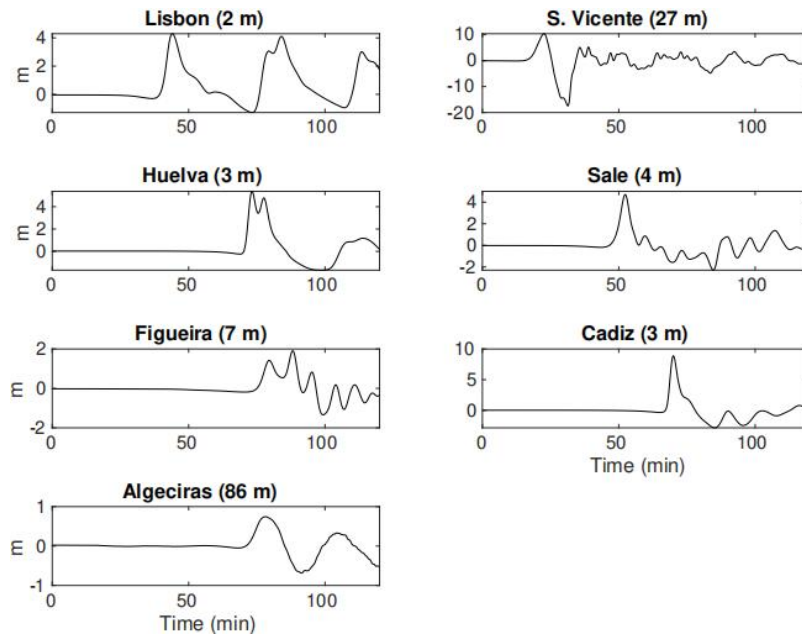
Figure 3. Time series of water elevations (m) at several locations indicated in Figure 2 after the 1755 Lisbon tsunami. The mean water depth of the grid cell where the gauge is located is indicated in parenthesis.

Calculated arrival times of the tsunami can be seen in Figure 4, where historical records are also shown. Calculations are in quite good agreement with these. The inundation caused by the tsunami is presented in Figure 5. All the coasts of Africa and Iberia were submerged greatly above 7 m. The largest runup occurred in the area of Cape San Vicente, above 20 m (historical records show that the runups here are larger than 10 m, but specific values are not provided). In the area of Cadiz (latitude 36.5°), historical records give a value of 15 m, in agreement with our calculations and in Lisbon (latitude 38.7°) 5 m, similar to our calculations (see Figure 5b) as well. Nevertheless, these results have to be interpreted as an estimation of the order of magnitude of the flood since a higher spatial resolution than the 30 s of arc used in the model is required for detailed runup calculations.
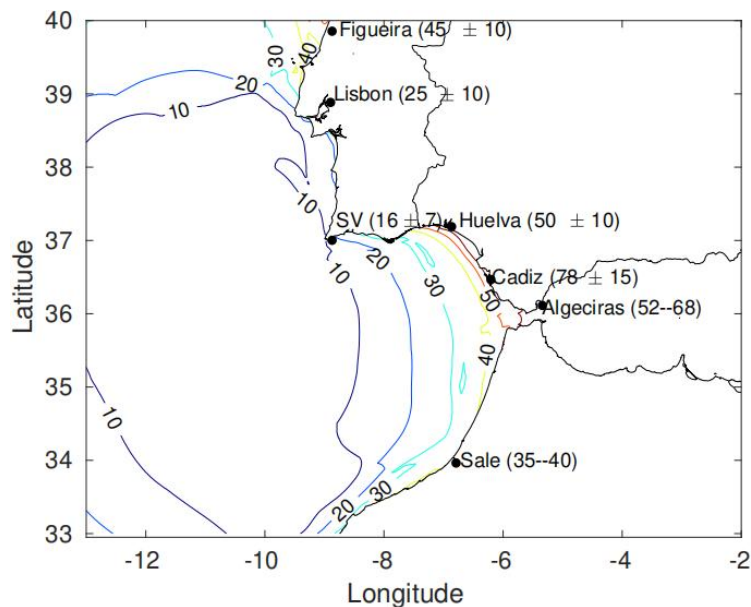
Figure 4. Calculated arrival times (min) for the 1755 Lisbon tsunami. Numbers in parenthesis indicate historical records of these times.
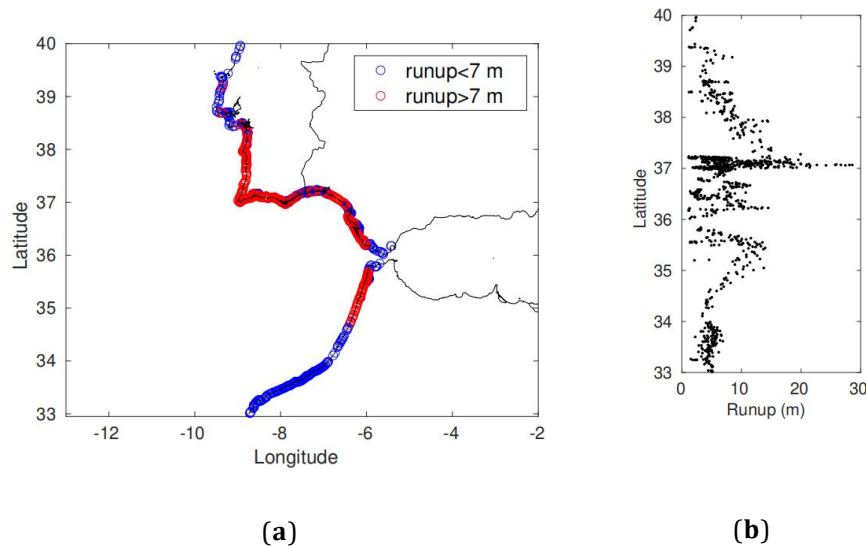
(**a**)   (**b**)

Figure 5. Calculated runups for the 1755 Lisbon tsunami. (**a**) shows cells flooded more and less than 7 m; (**b**) shows the calculated runup (m) as a function of latitude.

3.2. The 1856 Algeria Tsunami

An earthquake with an estimated magnitude of 7 occurred about 300 km east of Algiers on August 1856, generating a tsunami. The only historical data available consists of some reports on the damage which occurred along the Algerian coasts and in the Balearic Islands. The tsunami and its possible source were studied by Roger and Hébert [36] (see the 1856 tsunami in Table 2). The same source proposed by these authors was used in our model, which runs by using the ATWMED domain in Table 1.

The energy of this tsunami, as seen in Figure 6, presenting the computed wave amplitudes, is directed towards the near Algeria coast and the Balearic Island of Mallorca, although some waves also reach Menorca Island. Maximum wave height, however, is in the order of only 1 m, which is in agreement with the calculations shown in their study [36] (Figure 3 in reference [36]).
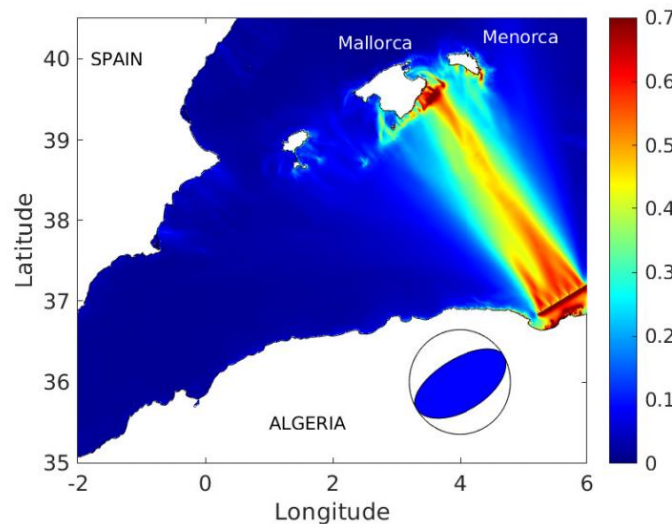

Figure 6. Computed wave amplitude (m) for the 1856 Algeria tsunami. The beachball corresponding to the source is drawn.

Calculated arrival times for this tsunami are drawn in Figure 7, although there is not any data to compare the results of our simulation. It can be seen that the tsunami takes less than one hour to reach the Balearic Islands and nearly two hours to reach the Spanish Mediterranean coast.
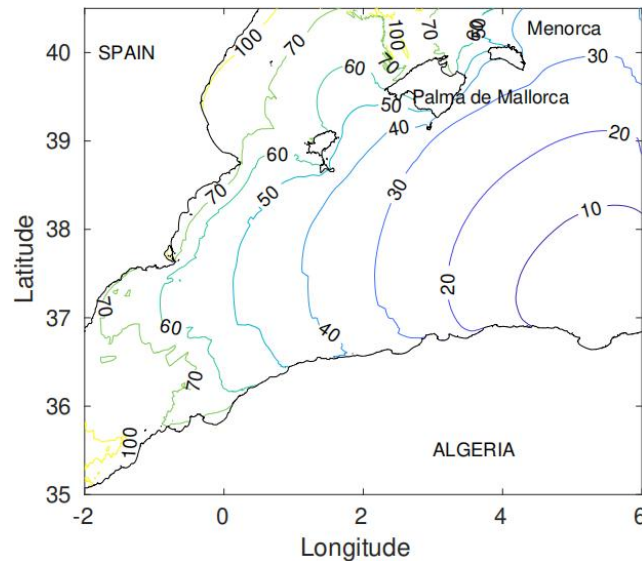
Figure 7. Calculated arrival times (min) for the 1856 Algeria tsunami.

3.3. The 2003 Algeria Tsunami

This tsunami was triggered by a 6.9 magnitude earthquake which took place on 21 May, its epicenter being located 50 km east from the city of Algiers. The ATWMED domain was used to simulate this tsunami again. Source parameters were used to describe the initial deformation (2003 tsunami in Table 2) [31].

The computed wave amplitudes are presented in Figure 8, which is in reasonable agreement with the previous calculation shown in reference [31] and also in reference [37] (Figures 6b and 5, respectively, in references [31] and [37]), which used the same source parameters. As shown in Figure 8, energy is directed towards the Balearic Islands again, but now Ibiza is more affected than Mallorca and Menorca. However, wave amplitudes are small, less than 0.5 m, which are underestimated for gauge measurements, as also happened in the previous calculations [31,37]. This was attributed to the effects of resonance in small bays [37], which cannot be solved by the coarse resolution (about 1 km) of the models, and also to a potential underestimation of the initial deformation caused by the earthquake.
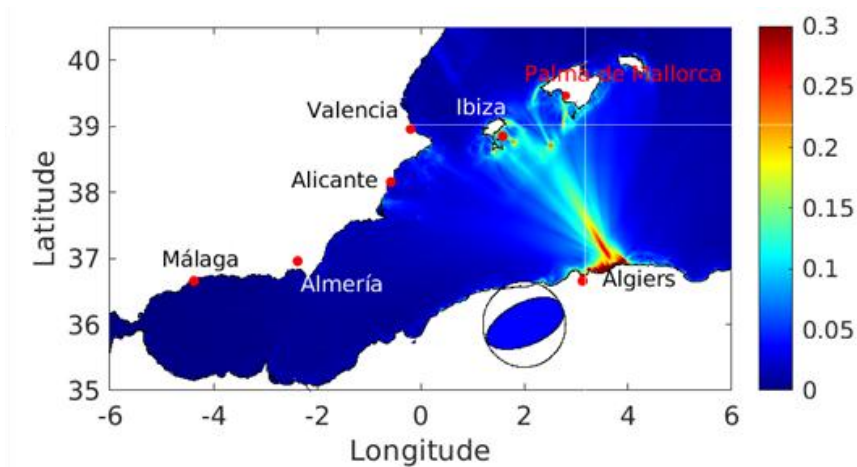

Figure 8. Computed wave amplitude (m) for the 2003 Algeria tsunami. The beachball corresponding to the source is drawn.

A comparison between computed arrival times of the tsunami and those registered by tidal gauges and the previous model can be seen in Table 3. Both sets of data are in reasonable agreement, especially when our results are compared with those of the model in the previous study [37]. The largest differences in arrival times

registered by tidal gauges appear in those for which sampling rates are larger: 10 and 5 minutes respectively in Algiers and Ibiza. The sampling rate in Palma de Mallorca was 1 minute (details can be seen in [37]). Thus, in the case of Algiers, presented results may be considered to be within the uncertainty range of measurements. Only in the case of Ibiza, the difference between the registered arrival time and the calculated arrival time is only a few minutes.

Table 3. Calculated and observed (or results of previous simulations) arrival times for the 2003 Algeria tsunami. Numbers in parenthesis are the results of Sahal et al. [37]. Locations are shown in the map in Figure 8.

Location	Arrival Time (min)	This Model (min)
Algiers	4	7
Palma de Mallorca	51	53
Ibiza	50	37
Valencia	(81)	81
Alicante	(70)	69
MÃ¡laga	(100)	104
AlmerÃa	(75)	76

3.4. Cyprus Tsunami, 1222

This tsunami was studied by Yolsal et al. [38], who provided the source parameters used as well in our model (see 1222 tsunami in Table 2), now running over the EASTMED domain. There are no historical records about the effects of this tsunami, but the results of our model are in good agreement with some previous calculations [38].

Calculated amplitudes are presented in Figure 9. Maximum amplitudes about 1 m are obtained in the source region, and energy is directed towards the Nile Delta. The Delta slows waves, which increase their amplitude here, as shown in Figure 9, and protects the coast of Egypt. This effect was also observed in the previous calculations [38] (Figure 8b in reference [38]). A map of calculated arrival times can be seen in Figure 10. There are no data or historical record to compare our results for these ancient tsunamis. In any case, it is understandable that the travel time from the source to the coast of Egypt is about one hour.
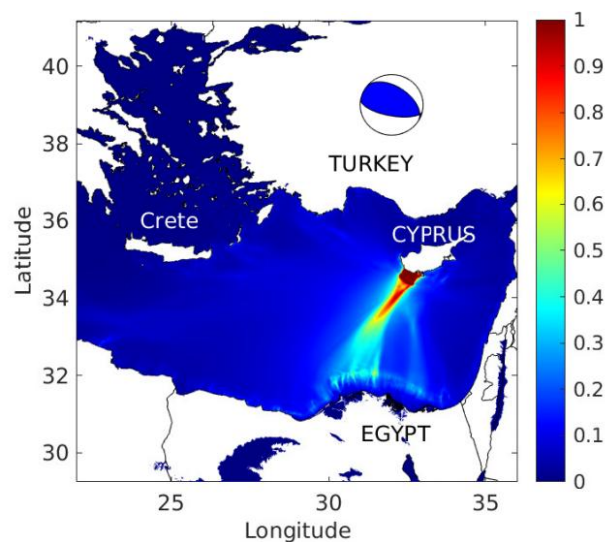

Figure 9. Computed wave amplitude (m) for the 1222 Cyprus tsunami. The beachball corresponding to the source is drawn.
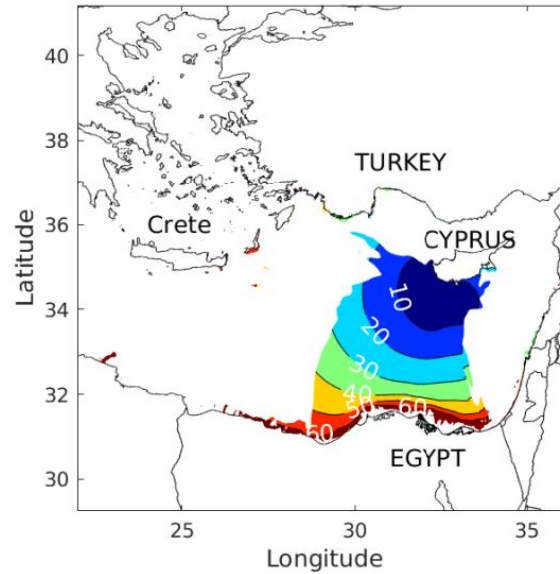
Figure 10. Calculated arrival times (min) for the 1222 Cyprus tsunami.

3.5. Crete, AD 365 Tsunami

Several authors have simulated this tsunami, caused by an 8.5 magnitude earthquake, by using slightly different source parameters [39,40]. We have used the source described in [41] (365AD tsunami in Table 2) over the EASTMED domain.

Wave amplitude is presented in Figure 11. It can be seen that most energy is directed to the southwest, with waves above 4 m along Libya coast and Crete, although significant waves also reach the islands of the Aegean Sea. These results are in good agreement with the earlier calculations [39] (Figure 5b in reference [39]).

The tsunami arrival times were also calculated and are presented in Figure 12, being in good agreement with those in reference [39] as well (Figure 5c in reference [39]). In particular, arrival times are about 30 minutes to the east coast of Lybia, about 90–100 minutes to the Nile Delta and 130 minutes to the east of Cyprus and the north of the Aegean Sea, in agreement with reference [39].
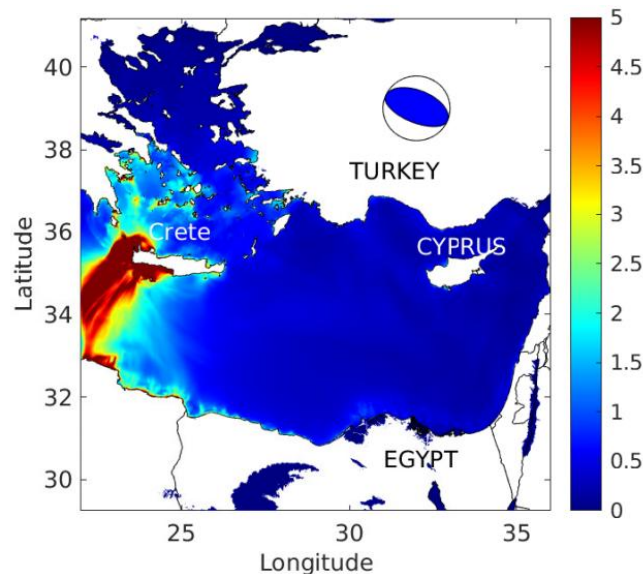

Figure 11. Computed wave amplitude (m) for the AD365 Crete tsunami. The beachball corresponding to the source is drawn.
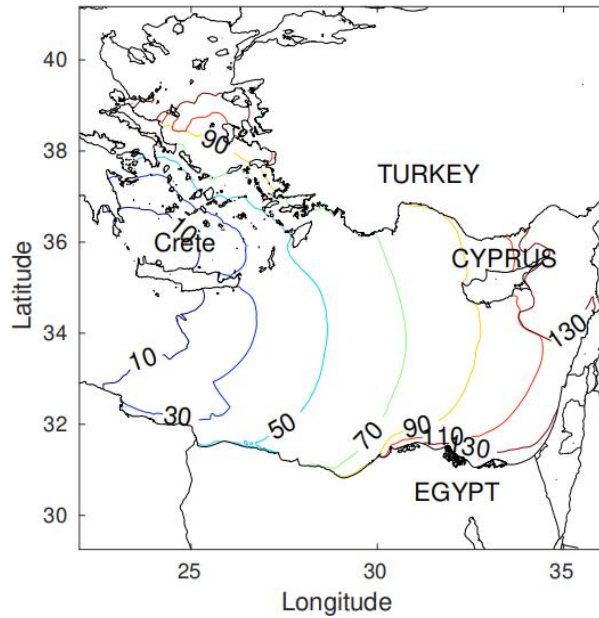
Figure 12. Calculated arrival times (min) for the AD365 Crete tsunami.

3.6. Crete, 1303 Tsunami

The source parameters, including location of the earthquake and its magnitude, are not clear. Source parameters have been proposed by different authors [38,40,42], and those of [38] were used in our model (see 1303 tsunami in Table 2).

Calculated wave amplitudes, shown in Figure 13, are in agreement with calculations in reference [38] (Figure 10b in reference [38]), using the same source parameters. The energy of the tsunami is directed to the southwest, as in the previous case, with waves above 1.5 m arriving to the coast of Libya. Waves about 5 m are obtained along the east coast of Crete, although they cannot be seen in Figure 13 due to the color scale.
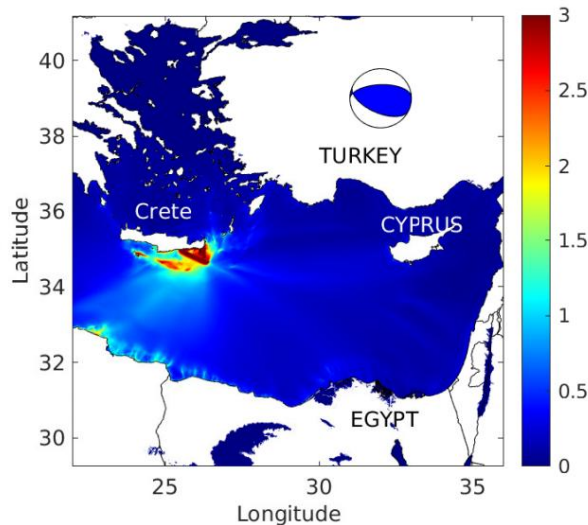

Figure 13. Computed wave amplitude (m) for the AD1303 Crete tsunami. The beachball corresponding to the source is drawn.

3.7. Rudbar Tsunami, 1990, Caspian Sea

The earthquake occurred in Iran on 20 June 1990, was one of the most destructive earthquakes registered in this country. Its source was investigated in [43], and values shown by these authors were used in our

simulations (1990 tsunami in Table 2). This simulation is used to check if the model was correctly customized to the Caspian Sea, and results were compared with the previous calculations in [43].

The epicenter of the earthquake was located inland (Figure 14) and the triggered tsunami was very small. Maximum displacements of the sea surface are a few cm along the southwest shore of the Caspian Sea and in the southeast corner, in agreement with the calculations in reference [43] (Figure 7a in reference [43]). However, several witnesses interviewed during a field survey [43] reported runup and inundation along the southern Caspian Sea shore. Thus, Salaree and Okal concluded that the reported tsunami was not directly caused by the earthquake, but by a submarine landslide triggered by it [43].
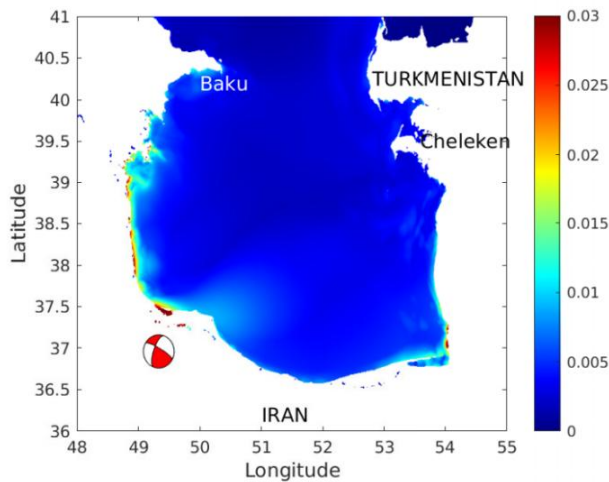

Figure 14. Computed wave amplitude (m) for the 1990 Rudbar tsunami. The beachball corresponding to the source is drawn at the epicenter location.

Although the tsunami due to the earthquake was actually negligible, this simulation was used, as mentioned above, to test the model in this area through its comparison with the earlier simulations [43].

3.8. The Krasnovodsk Earthquake, 8 July 1895, Caspian Sea

This was the largest earthquake in the Transcaspian region, which was studied in detail [44,45]. The triggered tsunami had not been simulated before. There is no clear data for the source mechanism of this earthquake, thus information given in Table 2 corresponds to plausible values determined in references [44,45]. Additionally, the Caspian Sea level was displaced 2 m upwards [44], since it was higher at such date, and the corresponding coastline was reconstructed. Actually, today's Cheleken Peninsula was an island at that time (see the island located at the west of the beachball in Figure 15).

There are no records of field surveys, but some historical notes suggest that the earthquake was followed by a tsunami which flooded Cheleken Island and other coastal areas [45,46].

Wave amplitudes are small, only within a limited region above 1 m, as shown in Figure 15. Since the tsunami was generated in very shallow water, the wave amplitudes decrease quickly as it propagates in the open waters of the Caspian Sea. Nevertheless, even these small waves were able to flood significant areas of Cheleken Island and the east shore of the Caspian Sea, at the east and south of Cheleken Island, which is in agreement with the mentioned historical notes. Actually, the land grid cells of the model domain, which were flooded by the tsunami at some time during the simulation, are shown in Figure 16.
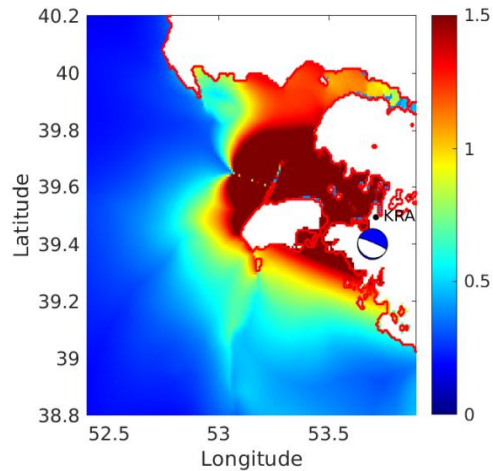
Figure 15. Computed wave amplitude (m) for the 1895 tsunami. The beachball corresponding to the source is drawn and the epicenter location is indicated by a black dot. The red line is the reconstructed 1895 coastline.
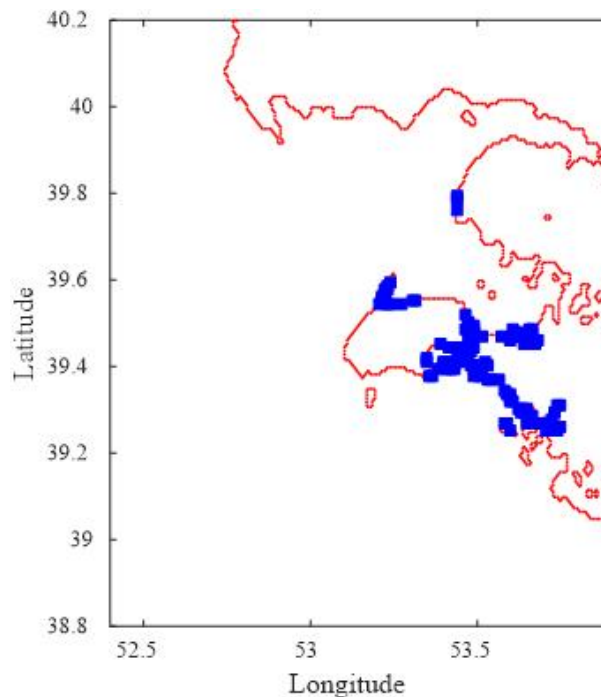

Figure 16. Inundation caused by the 1895 tsunami. The red line is the reconstructed 1895 coastline and blue squares indicate land cells which at some time were flooded.

3.9. The Late Bronze Age Eruption of Santorini and the Augias Megaturbidite

The Late Bronze Age (LBA) eruption of Thera (Santorini) is dated around 1613 BC. The decadence of the Minoan culture in the Aegean Sea and the biblical plagues of Egypt before the exodus of Israelites have been related with the LBA event since this was one of the largest Plinian eruptions occurring in the Earth in the last 10,000 years. A description of the eruption and the tsunami caused is given by Novikova et al. [23]: during the third phase of the eruption, the caldera collapsed and thick (up to some 55 m) pyroclastic flows entered into the sea, causing huge tsunamis. Only the tsunami due to the collapse of the caldera has been considered in this work.

The collapse volume was estimated to be in the range from 19 to 34 km^3 [23]. Our simulation uses a mean value of 26 km^3, similar to the 24 km^3 volume of Ozel et al. [47] and the 25 km^3 of Dominey-Howes [48]. Calculated amplitudes are presented in Figure 17; these are similar to those of reference [47] (Figure 8 in reference [47]). Waves over 7 m high reach the northern Crete coastline and some islands in the Aegean Sea. The

effects of the tsunami are limited to the southern Aegean Sea. Waves in the northern Aegean Sea suffer a strong attenuation; in addition, wave heights are not significant in the Eastern Mediterranean Sea. This is in agreement with the earlier calculations [47]. Actually, a high energy dissipation takes place in the narrow straits between the many islands in the sea. This effect was also found in the eastern Atlantic Ocean (see Figure 2): tsunamis generated by submarine earthquakes in the Gulf of Cádiz would not significantly propagate towards the Mediterranean Sea due to the high energy dissipation occurring along the narrow Strait of Gibraltar, which connects the Mediterranean Sea with the Atlantic Ocean.
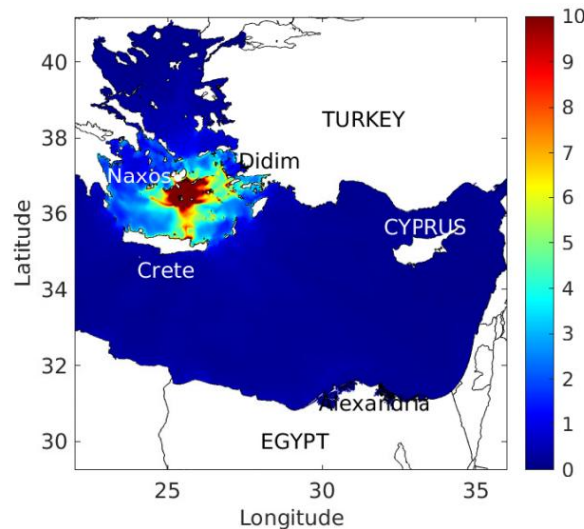

Figure 17. Calculated wave amplitudes (m) for the Santorini caldera collapse after a 3 hour simulation.

In this caldera collapse case, our results could be quantitatively compared with the previous simulation [23]. The comparison between the calculated amplitudes of both models at six locations in the Aegean Sea can be seen in Figure 18. Results are reasonably consistent., considering that two models are being compared among them and that collapsed volumes are not exactly the same (19 km^3 in reference [23]). Thus, there is obvious consistency between areas affected by small and large waves.
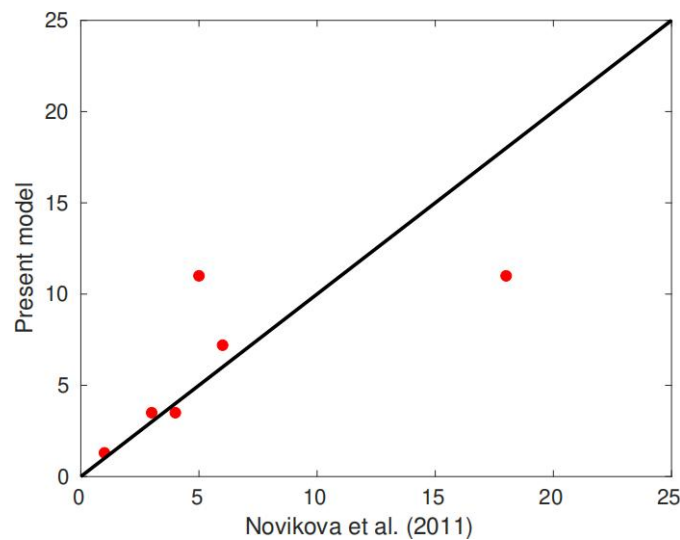

Figure 18. Comparison of calculated wave amplitudes (m) for the Santorini caldera collapse with the present model and that of Novikova et al. [23].

The intense flooding caused by the tsunami can be clearly seen in Figure 19, where calculated runups are presented. A large part of the north of Crete and most of the Aegean Sea islands were flooded more than 5 m; although part of the coast of Greece and Turkey was affected by flooding less than 5 m.
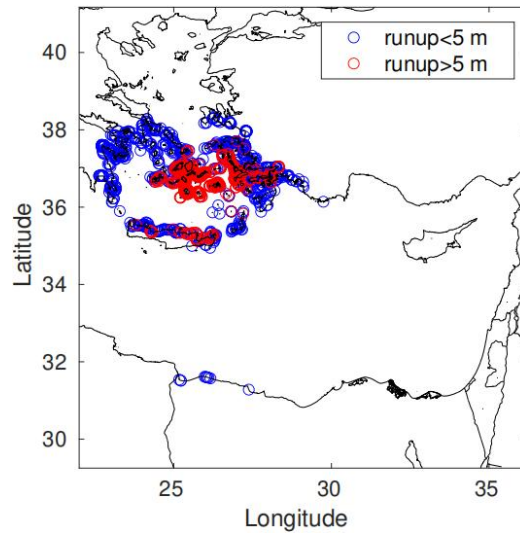

Figure 19. Calculated runups for the Santorini collapse.

Some time series of surface water elevations are presented in Figure 20. Initially, there is a recession of the sea level in all locations shown, especially in the Aegean Sea. Actually, it is larger than 15 m on the island of Naxos and about 10 m on the north shore of Crete. A large wave then arrives, about 10 m in both locations, which is followed by successive and smaller waves. The impact is smaller on the coast of Turkey, but still significant (waves higher than 2 m reach Didim). As mentioned before, little energy is able to exit from the Aegean Sea. Consequently, very small waves (less than 0.5 m) can reach Alexandria city in the north of Egypt.
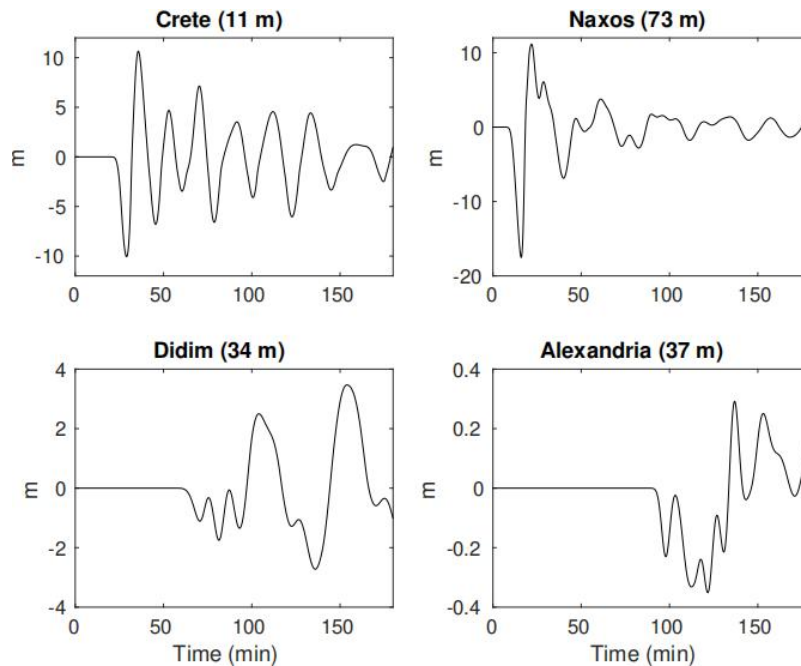

Figure 20. Time series of water elevations (m) at several locations indicated in Figure 17 after the Santorini collapse. The mean water depth of the grid cell where the gauge is located is indicated in parenthesis.

The sequence of tsunamis caused by the LBA eruption left geological fingerprints such as sedimentary deposits identified in the coasts of Turkey, Cyprus and Israel [23,49] and determined the time. However,

simulations indicate that the effects of the tsunamis were restricted to the Aegean Sea and thus such sedimentary deposits cannot be attributed to tsunamis directly triggered by the LBA eruption. Also, Cita and Rimoldi gave evidence of a 10–20 m thick megaturbidite existing in the Ionian Abyssal Plain (also known as Augias megaturbidite) which has an estimated volume of about 11 km³ [50]. Analysis of these deposits indicated that they were displaced from the Gulf of Sirte, in the African coast (see location in Figure 21) [51]. The LAB earthquake could have triggered a submarine landslide in the African shelf around the Gulf of Sirte: Cita and Rimoldi [50] suggested that the LBA tsunamis could have induced erosion and liquefaction of soft unconsolidated sediments and produced such a landslide. Nevertheless, previous results [23] and our results indicate that wave amplitudes out of the Aegean Sea are too small; although the landslide could have been triggered by seismic P-waves [52]. The coast of the Gulf of Sirte was analyzed to identify candidate locations for slope failures and to find suitable values for the landslide direction, dimensions, running distance and duration. One of the candidates was a slide with L_s = 16 km, B = 30 km, S = 2 km and Δz = 23 m, which gave a volume of 11 km³. The slide runs for 50 km with a maximum speed of 70 m/s. The CEMED domain was used to explore the tsunami due to this landslide.

Calculated amplitudes are presented in Figure 21. The tsunami impacts coastal areas in the north of Africa, western Greece, east of Sicilia and SW Italy. In particular, waves about 3 m reach part of eastern Sicilia. Thus, a sequential tsunami like this could have been the origin of the Augias megaturbidite and the sedimentary deposits, isochronous to the LBA eruption, which have been described in Augusta Bay. This is a clear example of how a research model can be used to evaluate the role of different candidate sources to produce a given fingerprint: in this case, if it was the tsunami produced by the LBA eruption or the tsunami due to a landslide triggered by the eruption the origin of the Augias megaturbidite in Sicily.
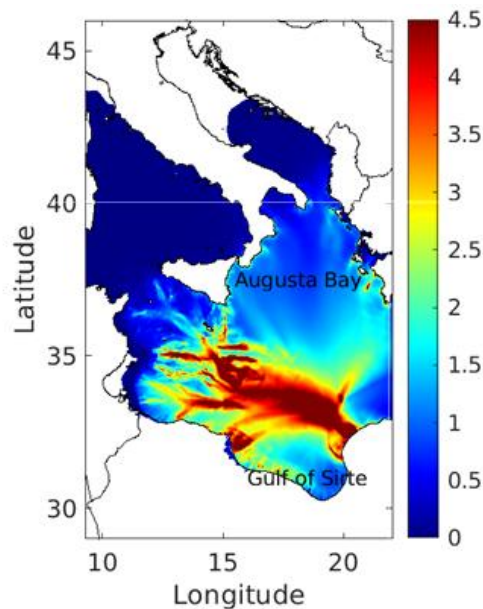

Figure 21. Calculated wave amplitudes (m) for the Sirte landslide after a 3 hours simulation.

3.10. The Akhziv Submarine Landslide

The 5 × 10 km Akhziv Canyon is located on the Levantine Mediterranean coast, in northern Israel. Salamon et al. suggested that the tsunami that followed the 1202 earthquake [53], with a rupture on land in Lebanon and northern Israel, was produced by a submarine landslide triggered by the earthquake, and proposed a landslide scenario for it. It consisted of a 18 m thick slide with length and width of 8 and 5 km respectively and with a smoothing distance of 25 km, which results in a volume equal to 2.47 km³ (Equation 13). The slide runs for 30 km in 0.21 hours, which provides a maximum velocity of 62 m/s [53].

Computed wave amplitudes are presented in Figure 22. They are higher than 4 m along the coast near the canyon (the color scale is limited to 2 m). Significant waves also arrive at the coastline along a 100 km line, in agreement with calculations in [53] (Figure 2 in this paper). Tsunami amplitude decreases rapidly as going far

from the canyon, since the source area of the tsunami is quite small. Thus, the rate of energy dissipation is faster than that of tsunamis from larger earthquake sources.
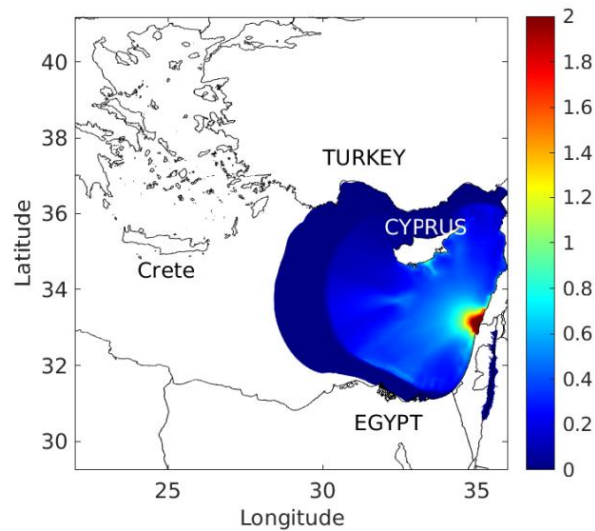

Figure 22. Calculated wave amplitudes (m) for the Akhziv submarine landslide after a 1-hour simulation.

3.11. The Former Gulf of Tartessos

The Gulf of Tartessos was located in SW Spain, between Cadiz and Huelva (see Figure 2), over the present-day Guadalquivir River valley. Today the Gulf is dry and forms the Guadalquivir marsh. There is evidence of a catastrophic tsunami, obtained through radiocarbon data, occurred in the range from 2700 to 2200 cal BP [54]. This lapse of time includes the collapse of the Tartessian culture, which took place around the sixth century BC. This culture flourished in the area around the first 1000 years BC under Phoenician influences. The pursuit of its capital, the lost city of Tartessos, has recently constituted one of the most exciting archaeological enterprises. It has been proposed that a catastrophic end of the Tartessian culture might have been caused by a tsunami that destroyed its capital city. In addition, the Atlantis of Plato might refer to the Tartessian culture [55].

The topography of the former Gulf, as it was about 2200 BP, was reconstructed to result in a quite shallow (mean depth about 2.5 m) and uniform water body with a central depression, to agree with the reconstruction in [56]. A Lisbon-like tsunami was then simulated (source details in Table 2) as the worst case. The modified ATWMED domain was used for this purpose.

Calculated wave amplitudes for such Lisbon-like tsunami in the former Gulf are presented in Figure 23. A significant reduction in wave amplitudes occurs inside the Gulf, which is due to energy dissipation in its entrance. Waves about 7 m high reach the open shoreline, but wave height quickly decreases in the Gulf connection with the open sea and amplitudes below 1 m are observed inside the Gulf of Tartessos. The morphological impacts of this tsunami are likely to include the erosion of coastal sediments and their subsequent spreading into the former Gulf. This tsunami would hardly produce any significant damage to the interior of the Gulf. A significant flooding would only occur along the boundary of the Gulf and the open Atlantic Ocean.
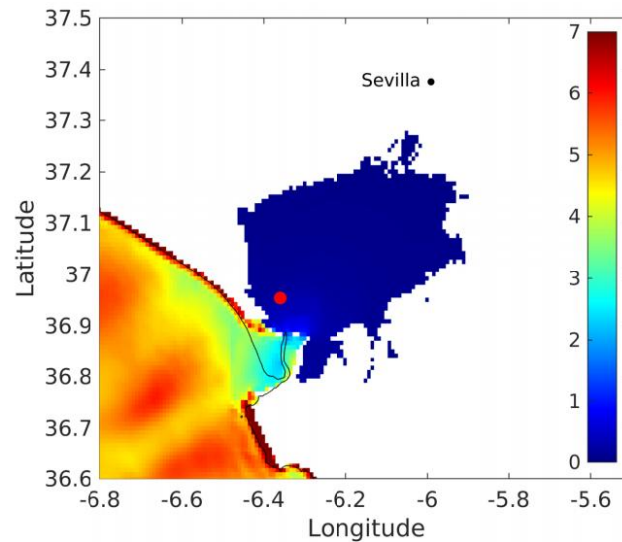
Figure 23. Calculated wave amplitude (m) for a Lisbon-like tsunami in the former Gulf of Tartessos after a 3-hour simulation. The red dot indicates the location proposed in reference [55] for the Tartessian capital city and the black line is the present-day coastline.

This is an example of how the present research model can be applied to discard unlikely scenarios of catastrophic floods attributed to tsunamis.

4. Discussion

As mentioned in the introduction, there are a number of available tsunami models, as listed in Table 1A in reference [2], where 27 models are cited (and it is not complete). The model used in this work is a research model developed in the University of Sevilla and successfully applied to past tsunamis in European waters. The model compares well with historical records (if they exist) and the results of other models.

In the study of historical tsunamis triggered by active faults or submarine landslides, it is challenging to get an accurate description of the complex heterogeneity of the source. In addition, instead of detailed records of water elevations, velocities, arrival times, and runups, the researcher usually handles sparse historical accounts and a few geological and/or archaeological fingerprints. In these cases, the classical Okada's formula for a single fault plane and a simple model of a sliding box have shown their use to provide a reasonable description of the main features of the tsunamigenic source, which (when nested into the hydrodynamic model) allows for an overall acceptable simulation of the tsunami propagation and its effects along the shoreline, as shown in wide sets of study cases presented in this work.

The main advantage of these research models is their flexibility to be adapted to different problems. For instance, the same code was applied to other problems related with flooding events. This is the case of the Bonneville Lake (USA) flood [28] and the Zanclean flood of the Mediterranean Sea [29], which occurred 5.3 Ma ago. A sediment transport model was later coupled to investigate the fate of the material which was eroded in the Strait of Gibraltar during the Zanclean flood [57].

Thus, these models may be customized to investigate other geological processes related to wave propagation and flooding. Of course, tsunami models are required to carry out risk assessment studies in areas prone to tsunamis [58,59] to develop suitable evacuation plans and to establish tsunami warning systems. As described in [60], the system for the eastern Mediterranean is based on sea bottom pressure gauges and optimizes gauge localization by the computation of possible tsunami scenarios.

Nevertheless, the limitations of the model should be commented as well. In particular, a simple flood/dry scheme was used, with more sophisticated descriptions, as described in [61]. Anyway, the spatial resolution of the model is not high enough to allow accurate runup calculations, as mentioned in the paper. Nested grids would be required for this purpose. For instance, 4 nested grids, with resolutions increasing from about 3 km to 250 m, are used in [62]. This possibility has not been achieved in our code yet. In addition, for tsunami earthquakes, the source has been modeled as a single fault plane, which is a common approach ([36,37,40,63]

among many others). However, a heterogeneous source consisting of a set of fault parameters, as done in reference [64] for instance, may be adequate if enough data is available.

Other topics for future improvements of the model are the consideration of non-hydrostatic pressure terms in the motion equations [65] and Earth's sphericity [66]. Nevertheless, spherical coordinates may be avoided in the present application cases of relatively small scale.

5. Conclusions

A research model to simulate the propagation of tsunamis is described. The model is based on the shallow-water hydrodynamic equations with non-linear terms, horizontal viscosity and friction with the seabed. Radiation conditions are used along open boundaries and a wet/dry algorithm is implemented along the shoreline. In the case of tsunamis produced by earthquakes, the initial sea floor deformation is calculated by using the classical formula of Okada, for which focal mechanisms must be provided. A rigid block model was used for the submarine landslide case and a simple depression of the sea surface for the volcano caldera collapse.

The model was tested through its application to historical tsunamis that occurred in European waters and comparisons of results with historical records and/or previous simulations, which is the objective of the this paper. The model was customized to four different domains for this purpose, covering the east Atlantic and the western Mediterranean, the eastern Mediterranean, the central Mediterranean and, finally, the Caspian Sea. Model results are, in general, in rather good agreement with available information. In addition, in the case of the Caspian Sea, the model was applied to simulate the Krasnovodsk tsunami of 1895, which has not been done before. Also, two examples of how these models can be applied to confront several candidate sources and to discard some unlikely scenarios of catastrophic floods attributed to tsunamis are presented: Santorini tsunami sequence including the origin of the Augias megaturbidite in east Sicily, and flooding of the former Gulf of Tartessos in SW Spain.

The authors hope that this work could encourage research groups to develop their own codes with the flexibility to be modified and applied to a large number of problems, without the need for commercial software.

Author Contributions

R.P., J.M.A., C.C.: conceptual and numerical models; software development; application, validation and discussion of results. R.P.: main writing. J.M.A., C.C.: review and editing.

Funding

No funding was received for conducting this study.

Institutional Review Board Statement

Not applicable.

Informed Consent Statement

Not applicable.

Conflicts of Interest

The authors have no competing interests to declare that are relevant to the content of this article.

References

1. Dias, F.; Dutykh, D. Dynamics of Tsunami Waves. In *Extreme Man-Made and Natural Hazards in Dynamics of Structures*; Ibrahimbegovic, A., Kozar, I., Eds.; Springer: Dordrecht, Netherlands, 2007; Volume 4, pp. 201–224. [CrossRef]
2. Marras, S.; Mandli, K.T. Modeling and Simulation of Tsunami Impact: A Short Review of Recent Advances and Future Challenges. *Geosciences* **2021**, *11*, 5. [CrossRef]
3. Allgeyer, S.; Cummins, P. Numerical Tsunami Simulation Including Elastic Loading and Seawater Density Stratification. *Geophys. Res. Lett.* **2014**, *41*, 2368–2375. [CrossRef]

4.   Dutykh, D.; Poncet, R.; Dias, F. The VOLNA Code for the Numerical Modeling of Tsunami Waves: Generation, Propagation and Inundation. *Eur. J. Mechanics-B/Fluids* **2011**, *30*, 598–615. [CrossRef]

5.   Scardino, G.; Rizzo, A.; Santis, V.D.; Kyriakoudi, D.; Rovere, A.; Vacchi, M.; Torrisi, S.; Scicchitano, G. Insights on the Origin of Multiple Tsunami Events Affected the Archaeological Site of Ognina (South-Eastern Sicily, Italy). *Quatern. Int.* **2022**, *638*, 122–139. [CrossRef]

6.   Baptista, M.A.; Miranda, J.M.; Chierici, F.; Zitellini, N. New Study of the 1755 Earthquake Source Based on Multi–Channel Seismic Survey Data and Tsunami Modelling. *Nat. Hazard. Earth Syst. Sci.* **2003**, *3*, 333–340. [CrossRef]

7.   Ioualalen, M.; Arreaga–Vargas, P.; Pophet, N.; Chlieh, M.; Ilayaraja, K.; Ordoñez, J.; Renteria, W.; Pazmiño, N. Numerical Modelling of the 26th December 2004 Indian Ocean Tsunami for the Southeastern Coast of India. *Pure Appl. Geophys.* **2010**, *167*, 1205–1214. [CrossRef]

8.   Lobkovsky, L.I.; Mazova, R.K.; Kisel'man, B.A.; Morozova, A.O. Numerical Simulation and Spectral Analysis of the November 15, 2006, Tsunami in the Kurile–Kamchatka Region. *Oceanology* **2010**, *50*, 449–458. [CrossRef]

9.   Kowalik, Z.; Murty, T.S. *Numerical Modelling of Ocean Dynamics*; World Scientific: Farrer Road, Singapore, 1993; 479p. [CrossRef]

10. Kampf, J. *Ocean Modelling for Beginners: Using Open-Source Software*; Springer Science & Business Media: Berlin/Heidelberg, Germany, 2009; 175p. [CrossRef]

11. Periáñez, R.; Casas-Ruíz, M.; Bolívar, J.P. Tidal Circulation, Sediment and Pollutant Transport in Cádiz Bay (SW Spain): A Modelling Study. *Ocean Eng.* **2013**, *69*, 60–69. [CrossRef]

12. Periáñez, R.; Pascual-Granged, A. Modelling Surface Radioactive, Chemical and Oil Spills in the Strait of Gibraltar. Comput. *Geosciences* **2008**, *34*, 163–180. [CrossRef]

13. Periáñez, R. Modelling the Environmental Behavior of Pollutants in Algeciras Bay (South Spain). *Mar. Pollut. Bull.* **2012**, *64*, 221–232. [CrossRef]

14. Periáñez, R. APERTRACK: A Particle–Tracking Model to Simulate Radionuclide Transport in the Arabian/Persian *Gulf. Prog. Nucl. Energy* **2021**, *142*, 103998. [CrossRef]

15. Periáñez, R. A Lagrangian Oil Spill Transport Model for the Red Sea. *Ocean Eng.* **2020**, *217*, 107953. [CrossRef]

16. Periáñez, R. Modelling the Transport of Suspended Particulate Matter by the Rhone River Plume (France). Implications for Pollutant Dispersion. *Environ. Pollut.* **2005**, *133*, 351–364. [CrossRef]

17. Periáñez, R. Environmental Modelling in the Gulf of Cadiz: Heavy Metal Distributions in Water and Sediments. *Sci. Total Environ.* **2009**, *407*, 3392–3406. [CrossRef]

18. Herzfeld, M.; Schmidt, M.; Griffies, S.M.; Liang, Z. Realistic Test Cases for Limited Area Ocean Modelling. *Ocean Model.* **2011**, *37*, 1–34. [CrossRef]

19. Okada, Y. Surface Deformation Due to Shear and Tensile Faults in a Half-Space. *Bull. Seismol. Soc. Am.* **1985**, *75*, 1135–1154. [CrossRef]

20. Wells, D.L.; Coppersmith, K.L. New Empirical Relationships Among Magnitude, Rupture Length, Rupture Width, Rupture Area and Surface Displacement. *Bull. Seismol. Soc. Am.* **1994**, *84*, 974–1002. [CrossRef]

21. Stirling, M.; Goded, T.; Berryman, K.; Litchfield, N. Selection of Earthquake Scaling Relationships for Seismic-Hazard Analysis. *Bull. Seismol. Soc. Am.* **2013**, *103*, 2993–3011.

22. Nomanbhoy, N.; Satake, K. Generation Mechanism of Tsunamis from the 1883 Krakatau Eruption. *Geophys. Res. Lett.* **1995**, *22*, 509–512. [CrossRef]

23. Novikova, T.; Papadopoulos, G.A.; McCoy, F.W. Modelling of Tsunami Generated by the Giant Late Bronze Age Eruption of Thera, South Aegean Sea, Greece. *Geophys. J. Int.* **2011**, *186*, 665–680. [CrossRef]

24. Tinti, S.; Pagnoni, G.; Zaniboni, F. The landslides and Tsunamis of the 30th of December 2002 in Stromboli Analyzed through Numerical Simulations. *Bull. Volcanol.* **2006**, *68*, 462–479. [CrossRef]

25. Cecioni, C.; Bellotti, G. Modeling Tsunamis Generated by Submerged Landslides Using Depth Integrated Equations. *Appl. Ocean Res.* **2010**, *32*, 343–350. [CrossRef]

26. Harbitz, C.B. Model Simulations of Tsunamis Generated by the Storegga Slides. *Mar. Geol.* **1992**, *105*, 1–21. [CrossRef]

27. Periáñez, R. Modelling the Suspended Matter Dynamics in a Marine Environment Using a Three Dimensional σ–Coordinate Model: Application to the Eastern Irish Sea. *Appl. Math. Model.* **2002**, *26*, 583–601. [CrossRef]

28. Abril-Hernández, J.M.; Periáñez, R.; O'Connor, J. E.; Garcia-Castellanos, D. Computational Fluid Dynamics Simulations of the Late Pleistocene Lake Bonneville Flood. *J. Hydrol.* **2018**, *561*, 1–15. [CrossRef]

29. Periáñez, R.; Abril, J.M. Computational Fluid Dynamics Simulations of the Zanclean Catastrophic Flood of the Mediterranean (5.33 Ma). *Palaeogeogr., Palaeoclimatol., Palaeoecol.* **2015**, *424*, 49–60. [CrossRef]

30. Jackson, J.; Priestley, K.; Allen, M.; Berberian M. Active Tectonics of the South Caspian Basin. *Geophys. J. Int.* **2002**, *148*, 214–245. [CrossRef]

31. Alasset, P. J.; Hébert, H.; Maouche, S.; Calbini, V.; Meghraoui, M. The Tsunami Induced by the 2003 Zemmouri Earthquake (MW = 6.9, Algeria): Modeling and Results. *Geophys. J. Int.* **2006**, *166*, 213–226. [CrossRef]

32. Matias, L.M.; Cunha, T.; Annunziato, A.; Baptista, M.A.; Carrilho, F. Tsunamigenic Earthquakes in the Gulf of Cadiz: Fault Model and Recurrence. *Nat. Hazards Earth Syst. Sci.* **2013**, *13*, 1–13. [CrossRef]

33. Scicchitano, G.; Gambino, S.; Scardino, G.; Barreca, G.; Gross, F.; Mastronuzzi, G.; Monaco, C. The Enigmatic 1693 AD Tsunami in the Eastern Mediterranean Sea: New Insights on the Triggering Mechanisms and Propagation Dynamics. *Sci. Rep.* **2022**, *12*, 9573. [CrossRef]

34. Baptista, M.A.; Miranda, P.M.A.; Miranda, J.M.; Mendes Victor, L. Constrains on the Source of the 1755 Lisbon Tsunami Inferred from Numerical Modelling of Historical Data on the Source of the 1755 Lisbon Tsunami. *J. Geodyn.* **1998**, *25*, 159–174. [CrossRef]

35. Barkan, R.; ten Brink, U.S.; Lin, J. Far field Tsunami Simulations of the 1755 Lisbon Earthquake: Implications for Tsunami Hazard to US East Coast and the Caribbean. *Mar. Geol.* **2009**, *264*, 109–122. [CrossRef]

36. Roger, J.; Hébert, H. The 1856 Djijelli (Algeria) Earthquake and Tsunami: Source Parameters and Implications for Tsunami Hazard in the Balearic Islands. *Nat. Hazard. Earth Syst. Sci.* **2008**, *8*, 721–731. [CrossRef]

37. Sahal, A.; Roger, J.; Allgeyer, S.; Lemaire, B.; Hébert, H.; Schindelé, F.; Lavigne, F. The Tsunami Triggered by the 21 May 2003 Boumerdes–Zmmouri (Algeria) Earthquake: Field Investigations on the French Mediterranean Coast and Tsunami Modelling. *Nat. Hazard. Earth Syst. Sci.* **2009**, *9*, 1823–1834. [CrossRef]

38. Yolsal, S.; Taymaz, T.; Yalciner, A.C. Understanding Tsunamis, Potential Source Regions and Tsunami–Prone Mechanisms in the Eastern Mediterranean. *Geol. Soc. Lond., Spec. Publ.* **2007**, *291*, 201–230.

39. Lorito, S.; Tiberti, M.M.; Basili, R.; Piatanesi, A.; Valensise, G. Earthquake-Generated Tsunamis in the Mediterranean Sea: Scenarios of Potential Threats to Southern Italy. *J. Geophys. Res.* **2008**, *113*. [CrossRef]

40. Yolsal, S.; Taymaz, T. Earthquake Source Parameters Along the Hellenic Subduction Zone and Numerical Simulations of Historical Tsunamis in the Eastern Mediterranean. *Tectonophysics* **2012**, *536–537*, 61–100. [CrossRef]

41. Stiros, S.C. The 8.5 Magnitude AD365 Earthquake in Crete: Coastal Uplift, Topography Changes, Archaeological and Historical Signature. *Quat. Int.* **2010**, *216*, 54–63. [CrossRef]

42. Hamouda, A.Z. Numerical Computations of 1303 Tsunamigenic Propagation towards Alexandria, Egyptian Coast. *J. Afr. Earth Sci.* **2006**, *44*, 37–44. [CrossRef]

43. Salaree, A.; Okal, E.A. Field Survey and Modelling of the Caspian Sea Tsunami of 1990 June 20. *Geophys. J. Int.* **2015**, *201*, 621–639. [CrossRef]

44. Ambraseys, N.N. The Krasnovodsk (Turkmenistan) Earthquake of 8 July 1895. *J. Earthquake Eng.* **1997**, *1*, 293–317. [CrossRef]

45. Balakina, L.M.; Moskvina, A.G. Seismogenic Zones of the Transcaspian Region: Characteristics of Sources of the Largest Earthquakes II. The Krasnovodsk and Kazandzhik Earthquakes. *Phys. Solid Earth* **2007**, *43*, 378–403. [CrossRef]

46. Kondorskaya, N.V.; Shebalin, N.V. *New Catalog of Strong Earthquakes in the USRR from Ancient Times Through 1977, Report SE-31*; World Data Center A for Solid Earth Geophysics: Boulder, Colorado, 1982; pp. 608.

47. Ozel, N.M.; Ocal, N.; Cevdet, Y.A.; Dogan, K.; Mustafa, E. 2011. Tsunami Hazard in the Eastern Mediterranean and Its Connected Seas: Towards a Tsunami Warning Center in Turkey. *Soil Dyn. Earthq. Eng.* **2011**, *31*, 598–610. [CrossRef]

48. Dominey-Howes, D. A Re–analysis of the Late Bronze Age eruption and Tsunami of Santorini, Greece, and the Implications for the Volcano-tsunami Hazard. *J. Volcanol. Geotherm. Res.* **2004**, *130*, 107–132. [CrossRef]

49. Goodman–Tchernov, B.N.; Dey, H.W.; Reinhardt, E.G.; McCoy, F.; Mart, Y. Tsunami Waves Generated by the Santorini Eruption Reached Eastern Mediterranean Shores. *Geology* **2009**, *37*, 943–946. [CrossRef]

50. Cita, M.B.; Rimoldi, B. Geological and Geophysical Evidence for the Holocene Tsunami Deposit in the Eastern Mediterranean Deep-sea Record. *J. Geodyn.* **1997**, *24*, 293–304. [CrossRef]

51. Shiki, T.; Cita, B. Tsunami–Related Sedimentary Properties of Mediterranean Homogenites as an Example of Deep-Sea Tsunamiite. In: *Tsunamites and Implications*, 1st ed.; Shiki, E.T., Tsuji, Y., Minoura, K., Yamazaki, T., Eds.; Elsevier: Amsterdam, Netherlands, 2008; pp. 203–215. [CrossRef]

52. Cita, M.B.; Camerlenghi, A.; Rimoldi, B. Deep–Sea Tsunami Deposits in the Eastern Mediterranean: New Evidence and Depositional Models. *Sediment. Geol.* **1996**, *104*, 155–173. [CrossRef]

53. Salamon, A.; Rockwell, T.; Ward, S.N.; Guidoboni, E.; Comastri, A. Tsunami Hazard Evaluation of the Eastern Mediterranean: Historical Analysis and Selected Modelling. *Bull. Seismol. Soc. Am.* **2007**, *97*, 705–724.

54. Lario, J.; Zazo, C.; Goy, J.L.; Silva, P.G.; Bardaji, T.; Cabero, A.; Dabrio, C.J. Holocene Palaeotsunami Catalogue of SW Iberia. *Quat. Int.* **2001**, *242*, 196–200. [CrossRef]

55. Kühne, R.W. Location and Dating of Atlantis. *Antiquity* **2004**, *78*, 300.

56. Rodríguez-Vidal, J.; Ruiz, F.; Cáceres, L.M.; Abad, M.; González-Regalado, M.L.; Pozo, M.; Carretero, M.I.; Monge Soares, A.M.; Toscano, F.G. Geomarkers of the 218–209 BC Atlantic Tsunami in the Roman Lacus Ligustinus (SW Spain): A Palaeogeographical Approach. *Quat. Int.* **2011**, *242*, 201–212. [CrossRef]

57. Periáñez, R.; Abril, J.M.; García-Castellanos, D.; Estrada, F.; Ercilla, G. An Exploratory Modelling Study on Sediment Transport during the Zanclean Flood of the Mediterranean. *SN Appl. Sci.* **2019**, *1*, 1–18. [CrossRef]

58. Otake, T.; Chua, C.; Suppasri, A.; Imamura, F. Justification of Possible Casualty-Reduction Countermeasures Based on Global Tsunami Hazard Assessment for Tsunami-Prone Regions over the Past 400 Years. *J. Disaster Res.* **2020**, *15*, 490–502. [CrossRef]

59. Okal, E.A.; Synolakis, C.E. Far-field Tsunami Hazard from Mega-Thrust Earthquakes in the Indian Ocean. *Geophys. J. Int.* **2008**, *172*, 995–1015. [CrossRef]

60. Wang, Y.; Heidarzadeh, M.; Satake, K.; Mulia, I.E.; Yamada, M. A Tsunami Warning System Based on Offshore Bottom Pressure Gauges and Data Assimilation for Crete Island in the Eastern Mediterranean Basin. *J. Geophys. Res-Sol. Ea.* **2020**, *125*. [CrossRef]

61. Gallardo, J.M.; Parés, C.; Castro, M.J. On a Well-Balanced High-Order Finite Volume Scheme for Shallow Water Equations with Topography and Dry Areas. *J. Comput. Phys.* **2007**, *227*, 574–601. [CrossRef]

62. Power, W.; Wang, X.; Lane, E.; Gillibrand, P. A Probabilistic Tsunami Hazard Study of the Auckland Region, Part I: Propagation Modelling and Tsunami Hazard Assessment at the Shoreline. *Pure Appl. Geophys.* **2013**, *170*, 1621–1634. [CrossRef]

63. Wang, Y.; Heidarzadeh, M.; Satake, K.; Hu, G. Characteristics of Two Tsunamis Generated by Successive M_w 7.4 and M_w 8.1 Earthquakes in the Kermadec Islands on 4 March 2021. *Nat. Hazards Earth Syst. Sci.* **2022**, *22*, 1073–1082. [CrossRef]

64. Lu, W.; Jiang, Y.; Lin, J. Modeling Propagation of 2011 Honshu Tsunami. *Eng. Appl. Comput. Fluid Mech.* **2013**, *7*, 507–518. [CrossRef]

65. Kämpf, J. *Advanced Ocean Modelling: Using Open-Source Software*, 1st ed.; Springer: Heidelberg, Germany, 2010; 181p. [CrossRef]

66. Khakimzyanov, G.; Dutykh, D.; Fedotova, Z. Dispersive Shallow Water Wave Modelling. Part III: Model Derivation on a Globally Spherical Geometry. *Commun. Comput. Phys.* **2018**, *23*, 315–360. [CrossRef]

Publisher's Note: The views, opinions, and information presented in all publications are the sole responsibility of the respective authors and contributors, and do not necessarily reflect the views of UK Scientific Publishing Limited and/or its editors. UK Scientific Publishing Limited and/or its editors hereby disclaim any liability for any harm or damage to individuals or property arising from the implementation of ideas, methods, instructions, or products mentioned in the content.